On the Origin of Atmospheric Frontal Lines off the East Coast of Taiwan Observed on Spaceborne Synthetic Aperture Radar Images

WERNER ALPERS

Institute of Oceanography, University of Hamburg, Hamburg, Germany

JEN-PING CHEN, CHIA-JUNG PI, AND I.-I. LIN

Department of Atmospheric Sciences, National Taiwan University, Taipei, Taiwan

(Manuscript received 3 March 2009, in final form 27 June 2009)

ABSTRACT

Frontal lines having offshore distances typically between 40 and 80 km are often visible on synthetic aperture radar (SAR) images acquired over the east coast of Taiwan by the *European Remote Sensing Satellites 1* and *2* (*ERS-1* and *ERS-2*) and *Envisat*. In a previous paper the authors showed that they are of atmospheric and not of oceanic origin; however, in that paper they did not give a definite answer to the question of which physical mechanism causes them. In this paper the authors present simulations carried out with the fifth-generation Pennsylvania State University–National Center for Atmospheric Research Mesoscale Model, which shows that the frontal lines are associated with a quasi-stationary low-level convergence zone generated by the dynamic interaction of onshore airflow of the synoptic-scale wind with the coastal mountain range of the island of Taiwan. Reversed airflow collides with the onshore-flowing air leading to an uplift of air, which is often accompanied by the formation of bands of increased cloud density and of rainbands. The physical mechanism causing the generation of the frontal lines is similar to the one responsible for the formation of cloud bands off the Island of Hawaii as described by Smolarkiewicz et al. Four SAR images are shown, one acquired by *ERS-2* and three by *Envisat*, showing frontal lines at the east coast of Taiwan caused by this generation mechanism. For these events the recirculation pattern, as well as the frontal (or convective) lines observed, were reproduced quite well with the meteorological model. So, it is argued that the observed frontal lines are not seaward boundaries of (classical) barrier jets or of katabatic wind fields, which have characteristics that are quite different from the flow patterns around the east coast of Taiwan as indicated by the SAR images.

1. Introduction

Frontal lines are frequently visible on synthetic aperture radar (SAR) images of the sea surface. They can be sea surface signatures of oceanic fronts as well as of atmospheric fronts or of convective lines. If no ancillary data are available, it is often quite difficult to determine whether they are of oceanic or atmospheric origin. Among the atmospheric phenomena that can give rise to frontal lines visible on SAR images of the sea surface are synoptic-scale fronts (see, e.g., Ivanov et al. 2004), land-breeze fronts (see, e.g., Sikora et al. 1996) and barrier jet fronts (see, e.g., Winstead et al. 2004, 2006). In a previous paper (Alpers et al. 2007) we have presented several SAR images acquired by the *European Remote Sensing Satellites 1* and *2* (*ERS-1* and *ERS-2*) over the east coast of Taiwan showing frontal features that closely follow the coastline and have offshore distances typically between 40 and 80 km. There we discarded the possibility that they are sea surface signatures of the Kuroshio front (an oceanic front). For this we checked the sea surface temperature and the surface current fields as provided online by the U.S. Naval Research Laboratory (see online at http://www7320.nrlssc.navy.mil/global_nlom32/taw.html) for a large number of SAR images on which frontal features are visible. We found that the positions of the frontal lines visible on the SAR images do not coincide with the Kuroshio front. Furthermore, the analysis of a large number of SAR images has revealed that the frontal lines are observed only under very specific meteorological conditions (i.e., when

Corresponding author address: Jen-Ping Chen, Department of Atmospheric Sciences, National Taiwan University, No. 1, Roosevelt Rd., Section 4, Taipei 10617, Taiwan.
E-mail: jpchen@as.ntu.edu.tw

DOI: 10.1175/2009MWR2987.1

a weak-to-moderate easterly wind blows against the mountain range at the east coast of Taiwan). The frontal lines separate areas of differing image brightness that results from differing sea surface roughness and thus from differing sea surface wind vectors. At the frontal lines the onshore airflow of the synoptic-scale wind collides with the offshore airflow, which gives rise to a convergence zone where air is forced to move upward. If the moisture content of the air is sufficiently high, clouds are formed. Thus the frontal lines are often associated with coast-parallel bands of increased cloud density, sometimes with rainbands.

The frontal lines are observed mostly on SAR images, which were acquired in winter and spring when a weak easterly wind is blowing against the mountain range. We have observed these frontal lines only when the component of the surface wind vector normal to the coast had values between 3 and 8 m s^{-1}. We will show that the frontal lines are associated with quasi-stationary low-level convergence zones generated by the dynamic interaction of onshore airflow with the coastal mountains of the island of Taiwan. The physical mechanism causing the generation of the frontal lines may be similar to the one responsible for the formation of cloud bands off the Island of Hawaii as described by Smolarkiewicz et al. (1988). Although the flow pattern at the east coast of Taiwan has some similarities with the flow pattern of barrier jets as observed off the southwest coast of Alaska (Overland and Bond 1993; Monaldo and Beal 2005; Loescher et al. 2006; Colle et al. 2006; Winstead et al. 2006), the SAR images reveal significant differences. In particular, the SAR images presented in this paper do not show strong alongshore winds at the southeast coast of Taiwan as one would expect when they were (classical) barrier jets.

Offshore frontal lines are not confined to the east coast of Taiwan, but have also been observed on many SAR images acquired over other sea areas bordered by coastal or near-coastal mountain ranges (e.g., off the east coasts of Vietnam, South Africa, and Mexico). In all cases, when frontal lines are visible on the SAR images, a weak to moderate wind (often the trade wind) was blowing against the coastal or near-coastal mountain range. The study of offshore frontal lines is not only of academic interest, but has also practical applications since it marks the distance up to which the offshore near-surface wind is blowing. This is of great value to sailors navigating sail boats in coastal waters and also to operators of incinerators located in coastal areas which emit noxious fumes into the air. Noxious waste should only be burnt at those times when the noxious fumes are not blown back onto shore.

In this study we present three SAR images that were acquired by the Advanced SAR (ASAR) on board the European *Envisat* satellite (launched on 1 March 2002) and one that was acquired by *ERS-2* (launched on 21 April 1995) over the east coast of Taiwan showing sea surface signatures of atmospheric frontal lines caused by the above-mentioned generation mechanism. To support our interpretation of the SAR images we have compared them with additional quasi-simultaneously acquired observational data. They include cloud images acquired by the Moderate Resolution Imaging Spectroradiometer (MODIS) on board the U.S. *Terra* satellite (more information is available online at http://modis.gsfc.nasa.gov and http://ladsweb.nascom.nasa.gov/data/search.html), sea surface wind field maps derived from the SeaWinds sensor on board the *Quick Scatterometer* (*QuikSCAT*) satellite (more information is available online at http://winds.jpl.nasa.gov/missions/quikscat/index.cfm and http://www.remss.com/qscat/qscat_browse.html), and weather radar data from the Central Weather Bureau of Taiwan.

In addition, we have carried out simulations for several events using the fifth-generation Pennsylvania State University–National Center for Atmospheric Research Mesoscale Model (MM5) with 24 vertical layers. We are aware that the MM5 model is probably not the best mesoscale atmospheric model for simulating the atmospheric phenomenon investigated in this paper. However, in our opinion it is well suited for the main purpose of this paper, which is to give an explanation for the physical mechanism leading to the formation of the atmospheric frontal lines visible on the SAR images. Obviously, higher-resolution atmospheric models, in conjunction with more detailed input data, will yield more detailed information on the frontal line, but we would like to leave this task to other investigators who have developed more sophisticated models.

The paper is organized as follows: First in section 2 we describe the MM5 model setup, and in sections 3–6 we present four SAR images showing radar signatures of atmospheric frontal lines off the east coast of Taiwan caused by airflow blocking. These SAR images are compared with ancillary data and MM5 simulation results. In section 7 the results are discussed in the light of theories of the interaction of airflow with mountains. To demonstrate that the frontal lines shown in sections 3–6 are quite different from those caused by katabatic winds, we present in section 8 a typical example of a katabatic wind front. In section 9 we summarize the main results of the paper.

2. The MM5 model setup

We have run the MM5 model with four levels of nested domains. From the outer to the inner domains, the horizontal grid resolutions are 45×45, 15×15, 5×5, and 1.7×1.7 km^2, and the number of grid points are

61 × 82, 79 × 88, 169 × 178, and 322 × 286, respectively. The domain center is set at 25.0°N, 118.0°E. In the vertical direction, 24 layers are used in the sigma coordinate system with σ = 1.00, 0.995, 0.99, 0.98, 0.96, 0.93, 0.89, 0.85, 0.80, 0.75, 0.70, 0.65, 0.60, 0.55, 0.50, 0.45, 0.40, 0.35, 0.30, 0.25, 0.20, 0.15, 0.10, 0.05, and 0.00. The vertical resolution is about 40 m at the lowest layer, and coarsens gradually to 500 m at the 700-hPa level. For the innermost domain, we have selected the ''simple ice'' explicit moisture and shallow convection options applied the cloud radiation scheme, the medium-range forecast (MRF) planetary boundary layer scheme, and the multilayer soil temperature scheme. Note that in this area of interest the weather is usually quite warm, thus the choice of ice-phase microphysical scheme is irrelevant. The initial and boundary conditions are derived from the National Centers for Environmental Prediction (NCEP) Aviation Model (AVN) data (see online at ftp://ftp.ncep.noaa.gov). All simulations were performed for a length of 72 h, starting 24 h ahead of the time period of interest.

In sections 3–6 we present simulation results carried out with this model for four different events for which we have SAR images showing pronounced radar signatures of frontal lines. However, in order not to overload this paper with plots, we only present a selection of plots that are essential for explaining the observations pertinent to the four events discussed. The first three events (18 January 1999, 11 December 2006, and 27 April 2007) are typical events in which the synoptic-scale wind blows with a speed of about 5 m s^{-1} almost normal to the mountain range, whereas the fourth event is somewhat exceptional, in which the synoptic-scale wind blows with a speed of about 8 m s^{-1} at an oblique angle from the northeast onto the mountain range.

3. The 18 January 1999 event

a. Observations

Figure 1 shows an *ERS-2* SAR image (swath width: 100 km; resolution: 25 m) acquired at 0225 UTC [1025 local standard time (LST)] on 18 January 1999. It shows a frontal line along the east coast of Taiwan at distances between 40 and 60 km from the base of the mountain range. Note that the roughness pattern east of this line, which is generated by the synoptic-scale wind, is much more homogeneous than the one west of it. The inhomogeneous roughness pattern possibly is caused by the large air–sea temperature difference leading to turbulence near the sea surface or by the inhomogeneous airflow generated by interaction of the synoptic wind with rough terrain. The semicircular features with dark patches visible in the northern section of the frontal line

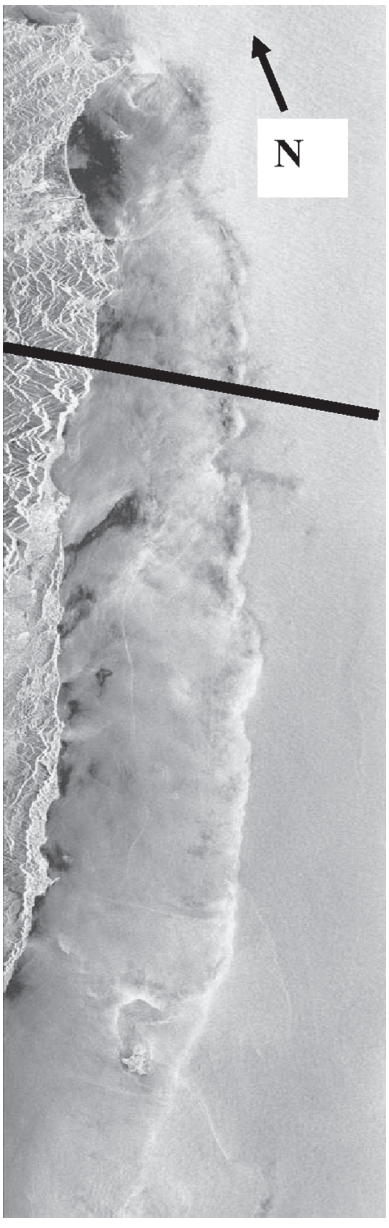

FIG. 1. *ERS-2* SAR strip acquired at 0225 UTC (1025 LST) 18 Jan 1999 over the east coast of Taiwan. The imaged area is 380 km × 100 km. The thick dark line inserted in the SAR image denote the transect along which vertical profiles of streamlines and cloud water density are calculated by using the MM5 model (see Fig. 2).

are typical sea surface manifestations of convective rain cells (Atlas 1994; Melsheimer et al. 2001; Alpers and Melsheimer 2005). Note that in this SAR image the frontal line shows up over large distances as a bright line, which implies that the radar backscattering there is enhanced relative to the background. However, as will be shown in the model simulation, winds at this conversion line are relatively weak thus unable to generate strong

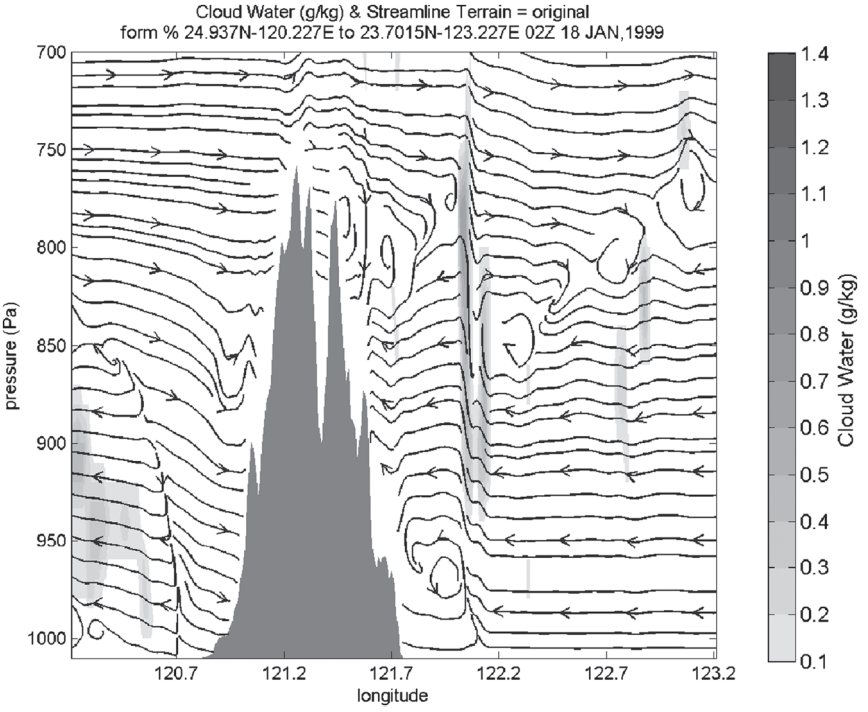

FIG. 2. Vertical cross section of the simulated streamlines and cloud water content (gray shading; g kg^{-1}) along a transect through northern Taiwan at 0200 UTC 18 Jan 1999.

waves to cause the high backscattering. A likely reason is that in this case the surface waves, which are generated by the two opposing wind systems and that propagate in opposite directions, interact so strongly and nonlinearly that they break. This would result in an increase in the sea surface roughness and thus to an increase in radar backscattering (cf. van Vledder and Holthuijsen 1993). But another possible cause for the frontal line to show up as a bright line on the SAR image is that it is also the boundary between two areas of different stabilities of the near-surface air layer. Toward the coast (to the west) this layer is highly unstable, while toward the open sea (to the east) it is neutrally stable as evidenced by the homogeneous brightness pattern. We expect that at this boundary strong turbulence is encountered, which gives rise to an increase in the sea surface roughness and thus to an increase in radar backscattering.

Cloud images taken from the Japanese *Geostationary Meteorological Satellite 4* (*GMS-4*) in the visible band between 0233 and 0833 UTC 18 January 1999 (not reproduced here, but two of them were shown in Alpers et al. 2007) show pronounced coast-parallel cloud bands that closely follow the position of the frontal line visible on the SAR image. The persistence of the cloud band over 6 h into the late afternoon clearly demonstrates that the generation of the frontal line cannot be attributed to the interaction of the synoptic-scale wind with a katabatic wind, which is present only late in the evening, at night, and early in the morning. The surface weather map at 0000 UTC 18 January (not reproduced here) shows east of Taiwan winds of 5 m s^{-1} from the southeast, cloud coverage of 7/8, and rain showers. West of Taiwan it shows winds of 2.5 m s^{-1} from the north-northeast. The 850-hPa weather map shows a westerly wind aloft. The radiosonde launched at Hualien, a coastal city at the east coast of Taiwan, measured at 0000 UTC 18 January at a height of 19 m a wind speed of 2.6 m s^{-1}, a wind direction of 240°, an air temperature of 16.7°C, and a relative humidity of 94%. The water temperature was around 24°C.

b. Simulations

The results of the simulations carried out with the MM5 model for the 18 January 1999 event are depicted in Figs. 2–4. The plot depicted in Fig. 2 shows the vertical cross section of the simulated streamlines and of the cloud water content along a transect through northern Taiwan (the transect is inserted in Fig. 1 as a dark line). Clearly visible on this plot is the recirculation pattern east of the mountain range. When the prevailing airflow from the east encounters the mountain range, the lower-level airflow curls down, forms a vortex roll (or band) and thus generates a reverse flow near the sea surface. This return flow meets the onshore airflow at about

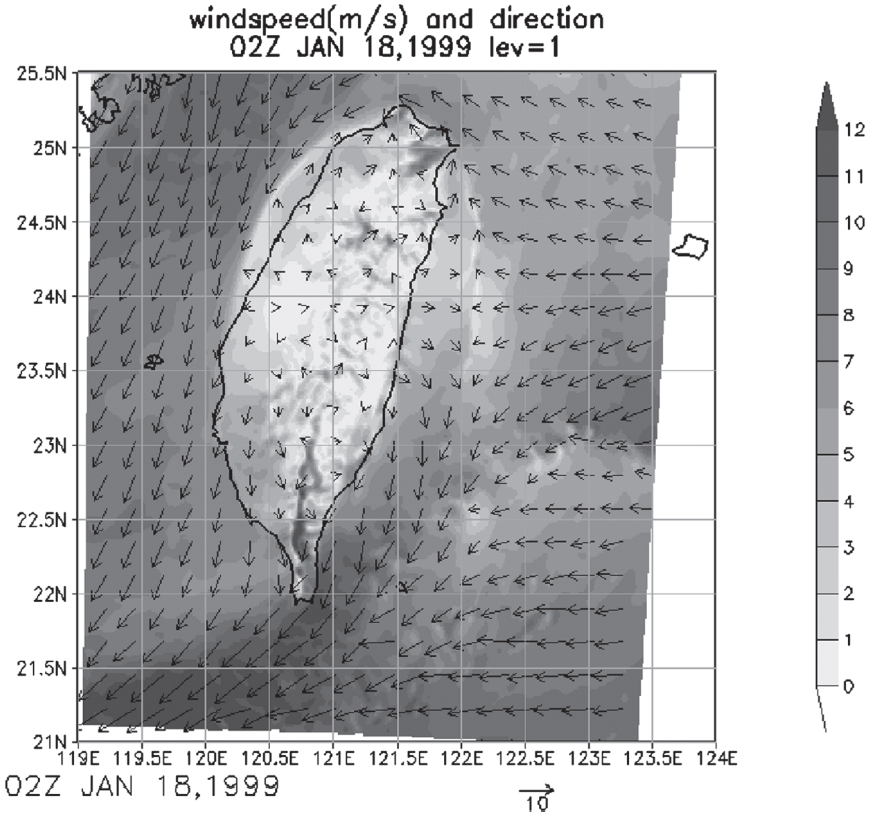

FIG. 3. Simulated wind velocity (vectors) and wind speed (grayscale shading; m s^{-1}) at the lowest model level at 0200 UTC 18 Jan 1999.

40 km offshore and forms a convergence zone. The onshore flow is lifted upward by the return flow at the convergence zone. When the uplifted air reaches the condensation level, clouds develop above the convergence zone. But sometimes clouds develop also at other locations: 1) at the top of the mountain range due to orographic lifting of the upper part of the onshore airflow (see Figs. 9 and 10), and 2) farther upstream (see Figs. 2, 9, and 13) possibly due to forced wave motion. Note that at higher levels the wind is blowing from the west, which means that no air from the east is flowing over the mountain range at this location. These phenomena persisted for more than 24 h with slight variations in location and strength.

The plot depicted in Fig. 3 shows the simulated wind velocity (vectors) and wind speed (shadings) calculated for the lowest level at 0200 UTC 18 January 1999. The wind speed is given in the grayscale in meters per second. The plot shows that the airflow of the easterly synoptic-scale wind is blocked by the mountain range, splits and flows around Taiwan, and then rejoins on the lee side. This flow behavior is similar to the one encountered for flow past an isolated island as described by Smolarkiewicz et al. (1988) for low Froude numbers. A closer look at this plot reveals that in the central northern section an offshore airflow leaves the eastern coastline and moves against the airflow of the synoptic-scale easterly wind. This offshore flow forms the return flow that, when it encounters the onshore flow, generates an atmospheric convergence line. Sometimes the sea surface roughness is increased in the convergence zone, but more often it is decreased relative to the background. In this first case the frontal line shows up as a bright line on the SAR image but in the next case as a dark boundary. The simulations show further that in the southern section of the image the airflow is deflected southward along the coastline, which would suggest the formation of a barrier jet. Unfortunately, the SAR image in Fig. 1 did not cover this area thus provided no verification.

On the SAR image the coast-parallel roughness band shows up as an area of quite high image brightness suggesting high wind speeds. But this interpretation is not correct because the model function that is usually used for converting radar image brightness into wind speed (see next section) does not apply in this case because the water temperature was much higher (24°C) than the air temperature (16.7°C). This implies that the air layer near the sea surface was highly unstable, favoring

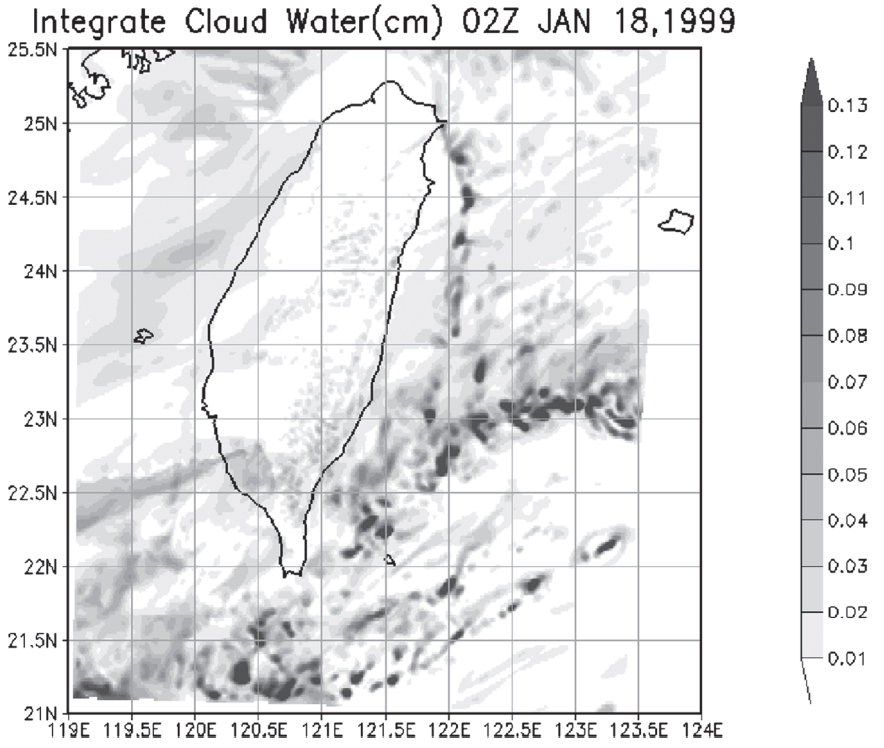

FIG. 4. Map of the simulated integrated cloud water content (cm) at 0200 UTC 18 Jan 1999.

turbulence and thus an increase in sea surface roughness. Since SAR measures wind speed via sea surface roughness, the high sea surface roughness leads us to believe that here the wind speed was higher than it actually was (in this case 2–3 m s^{-1} higher). For more details on the dependence of the radar backscatter from the sea surface on air–sea temperature difference the reader is referred to the paper by Keller et al. (1989).

Figure 4 shows a plot of the integrated cloud water (vertically integrated amount of cloud water given as a depth of water in centimeters) for 0200 UTC 18 January 1999. Visible is a band of increased cloud water located off the east coast of north Taiwan whose location corresponds approximately to the position of the frontal line visible on the SAR image. Areas of increased integrated cloud water are potential areas of rain. Since the semicircular features with dark patches visible in the center visible in the upper (northern) section of the SAR image (Fig. 1) are located in an area of increased integrated cloud water (Fig. 4), we take this as additional evidence that they are radar signatures of rain cells.

4. The 11 December 2006 event

a. Observations

Figure 5 (left panel) shows a section of an *Envisat* ASAR wide swath image acquired at 1401 UTC (2201 LST) 11 December 2006. The right panel shows the sea surface wind field derived from the ASAR image. When retrieving wind fields from SAR images, one first has to convert image brightness into normalized radar cross section (NRCS) and then NRCS into wind speed by using a wind scatterometer model function. Here we use the C-band scatterometer model, version 4 (CMOD4), model function. It relates NRCS values of a C-band radar image to wind speed and direction at a height of 10 m above the sea surface when the air above the sea surface is neutrally stable (water and air temperatures are equal; Stoffelen and Anderson 1997). Since the NRCS depends on both wind speed and relative angle between look direction of the SAR antenna and wind direction, and since SAR measures the NRCS only at one direction (normal to the flight direction), one has to get the wind direction from another source (see, e.g., Alpers et al. 2009). In this investigation we take the wind direction from the NCEP atmospheric model, which provides globally ocean surface wind fields at a grid spacing of 0.5° every 3 h. However, the wind directions of the NCEP model are often not accurate enough (due to the coarse spatial and temporal resolution) to retrieve finescale structures (of the order of hundreds of meters to tens of kilometers) of wind fields from SAR images. An alternative method is to take wind directions from higher-resolution atmospheric models that are tailored

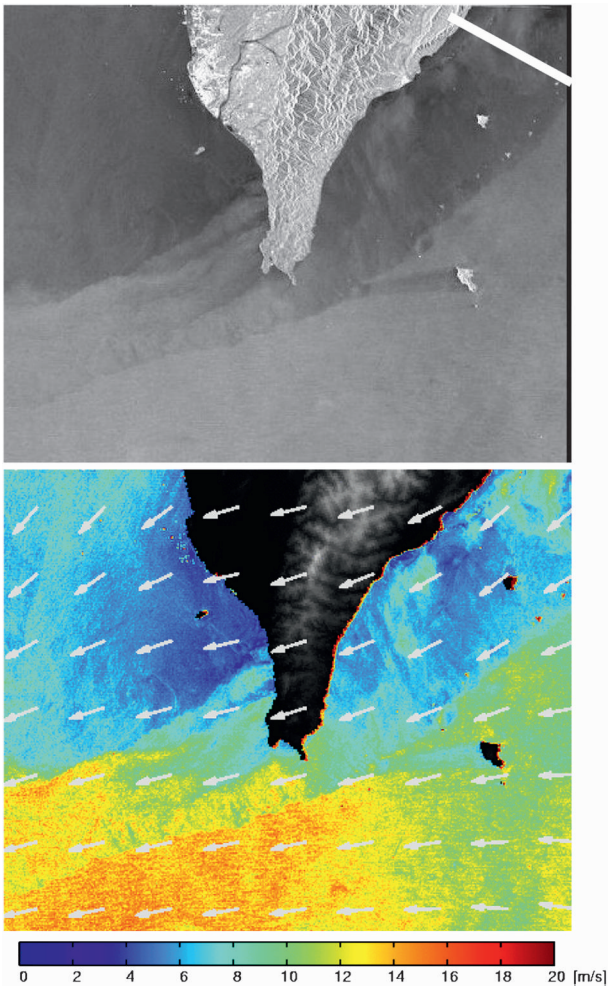

FIG. 5. (top) *Envisat* ASAR wide swath image acquired at 1401 UTC (2201 LST) 11 Dec 2006. The imaged area is 230 km by 205 km. (bottom) Sea surface wind field derived from the ASAR image by taking the wind direction from the NCEP model and by using the CMOD4 wind scatterometer model. The thick white line inserted in the ASAR image denotes the transect along which vertical profiles of streamlines and cloud water density are calculated using the MM5 model (see Fig. 9). The two bright spots visible on the ASAR image east of Taiwan are the islands Lutao to the north and Lanyu to the south.

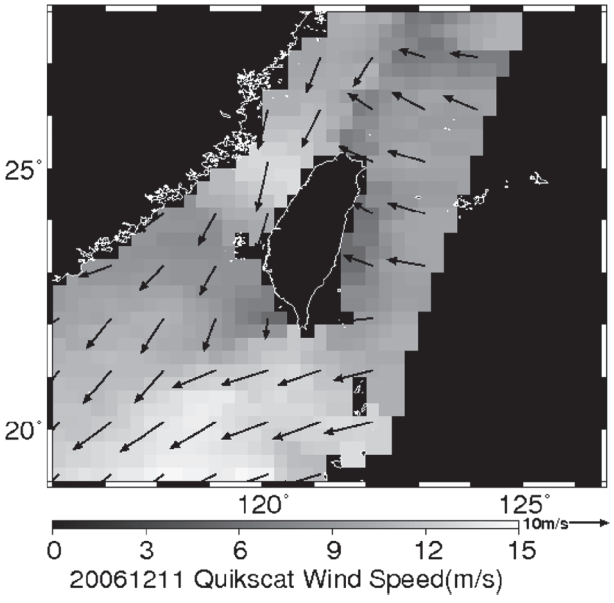

FIG. 6. Sea surface wind field derived from *QuikSCAT* data acquired at 1048 UTC 11 Dec 2006.

to study specific mesoscale atmospheric phenomena. But a better method is to use the information on wind direction that is contained in the SAR image. Such information is provided by linear features that are sometimes visible on SAR images of the sea surface, such as wind streaks, roll vortices, and wakes behind coastal mountains and islands (Monaldo and Beal 2005; Horstmann and Koch 2005; Alpers et al. 2009).

The ASAR-derived wind field map (Fig. 5) shows that at the east side of the southern tip of Taiwan a synoptic-scale wind with a speed of about 10–12 m s^{-1} was blowing from the northeast. This wind direction is in agreement with the direction inferred from the direction of the wind shadow behind the island of Lanyu (the most southerly island visible on the ASAR image as a dark patch). On the other hand, the wind field map derived from *QuikSCAT* data (Fig. 6) shows a synoptic-scale wind of about 10 m s^{-1} blowing from a more easterly direction. But these data were acquired 3 h and 13 min before the ASAR data acquisition. An interesting feature visible on the *QuikSCAT* wind field map is the low wind speed area near the coast. However, no reliable wind fields near coastlines can be derived from *QuikSCAT* data, which has a resolution of only 25 km. This is why on the high-resolution (12.5 km) *QuikSCAT* wind field plots distributed by National Oceanic and Atmospheric Administration/National Environmental Satellite, Data, and Information Service (NOAA/NESDIS, more information is available online at http://manati.orbit.nesdis.noaa.gov/hires/) no wind vectors are shown in 25–50-km-wide bands adjacent to coastlines. Obviously, the wind field plot depicted in Fig. 6 (which was obtained from http://www.remss.com/qscat/qscat_browse.html) shows wrong wind directions near the east coast of Taiwan.

The most noticeable feature in this SAR image is the dark band, approximately 55 km wide, stretching along the eastern coast of Taiwan indicating that the sea surface wind speed there is considerably lower (between 4 and 8 m s^{-1}) than the speed of the synoptic wind farther east (between 10 and 12 m s^{-1}). This is confirmed by meteorological measurements carried out at the island of Lutao, which lies in the low wind speed area adjacent to the coast and is visible as a small dark patch in the

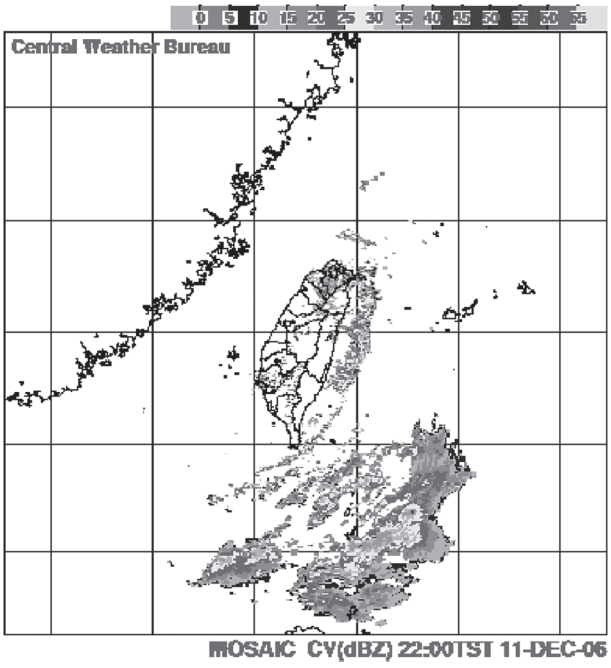

FIG. 7. Weather radar image acquired at 1400 UTC 11 Dec 2006.

upper-right-hand section of the ASAR image. There a wind speed of 5 m s^{-1} and a wind direction of 30° were measured at ground level at 1200 UTC 11 December 2006. Thus we have for this event evidence from three different sensors (ASAR on *Envisat*, SeaWinds on *QuikSCAT*, and an anemometer on the island of Lutao) that the sea area adjacent to the coast is a low wind speed and not a high wind speed area, which would be indicative of a barrier jet. Thus, the frontal line separating sea areas of differing sea surface roughness cannot be interpreted as the seaward boundary of a barrier jet. Note also the bright spots along the line separating the dark area from the brighter area farther east, which are radar signatures of rain cells. It seems strange that the small rain cells show up on this SAR image as small bright spots and not as dark spots as reported by Atlas (1994). Evidence that the bright spots are indeed radar signatures of rain cells is provided by the quasi-simultaneously acquired weather radar image depicted in Fig. 7. We interpret these radar signatures as being caused by scattering at raindrops in the atmosphere and not by scattering at the sea surface, where the impinging raindrops modulate the small-scale sea surface roughness.

The weather radar image depicted in Fig. 7, which was acquired almost at the same time (1415 UTC) as the ASAR image (1401 UTC), shows a rainband that extends along the east coast at an offshore distance of about 60 km. The rainband is broad in the northern section and quite narrow in the southern section. Inspection of the time series of the weather radar images (not reproduced here) reveals that the rainband was present over a time period of more than 24 h (from 0600 UTC 11 December to 0800 UTC 12 December). Figure 8 shows the weather radar image acquired at 0200 UTC on the same day (left panel) together with the MODIS *Terra* image acquired 15 min later (right panel). Again, on the weather radar image a coast-parallel rainband is visible, which corresponds quite well to the band of increased cloud density visible on the MODIS image in the central section of Taiwan. Visible also on the MODIS image are clouds above the coastal mountains. The radio sounding data acquired at 0000 UTC 11 December 2006 at Taipei (a city located in northern Taiwan) and Ishigakijima (an island near the eastern boarder of Fig. 8, the nearest offshore sounding station available to us) both show that aloft (above 3100 m) a westerly-to-southwesterly wind was blowing. The water temperature was 26°C and the air temperature at Ishigakijima was 26.6°C and at Taipei 26.8°C. The 850-hPa weather map shows an easterly wind crossing Taiwan aloft.

b. Simulations

The results of the simulations carried out with the MM5 at 1400 UTC 11 December 2006 event are depicted in Figs. 9–11, showing vertical cross sections of simulated streamlines and water content along transects through southern and central Taiwan cutting the mountain range at vertical angles. The transect through southern Taiwan is inserted in Fig. 5 as a white line. As in the previous event (Fig. 2), recirculation patterns are visible in this event (Figs. 9 and 10). The return flow meets the onshore airflow at about 60 km from the base of the mountain range and forms a convergence zone. However, the simulations show significant differences for the two transects through central and southern Taiwan. On the transect through southern Taiwan, the center of the vortex roll is located at a lower level (about 300 m above sea level) than on the transect through central Taiwan (about 1100 m above sea level). Furthermore, in the south the easterly airflow crosses over the mountain range, whereas in the center it does not. Only at those locations where the height of the mountain range is sufficiently low (approximately 600 m) can the airflow from the east cross it. This can also be seen on the ASAR image depicted in Fig. 5, where west of the southern tip of Taiwan the wind blows much more strongly than in the area farther north at the west coast, where the airflow from the east is blocked by the higher mountains. Another difference revealed by these plots is that in the south the cloud band is much narrower than in the center. These simulation results are supported by

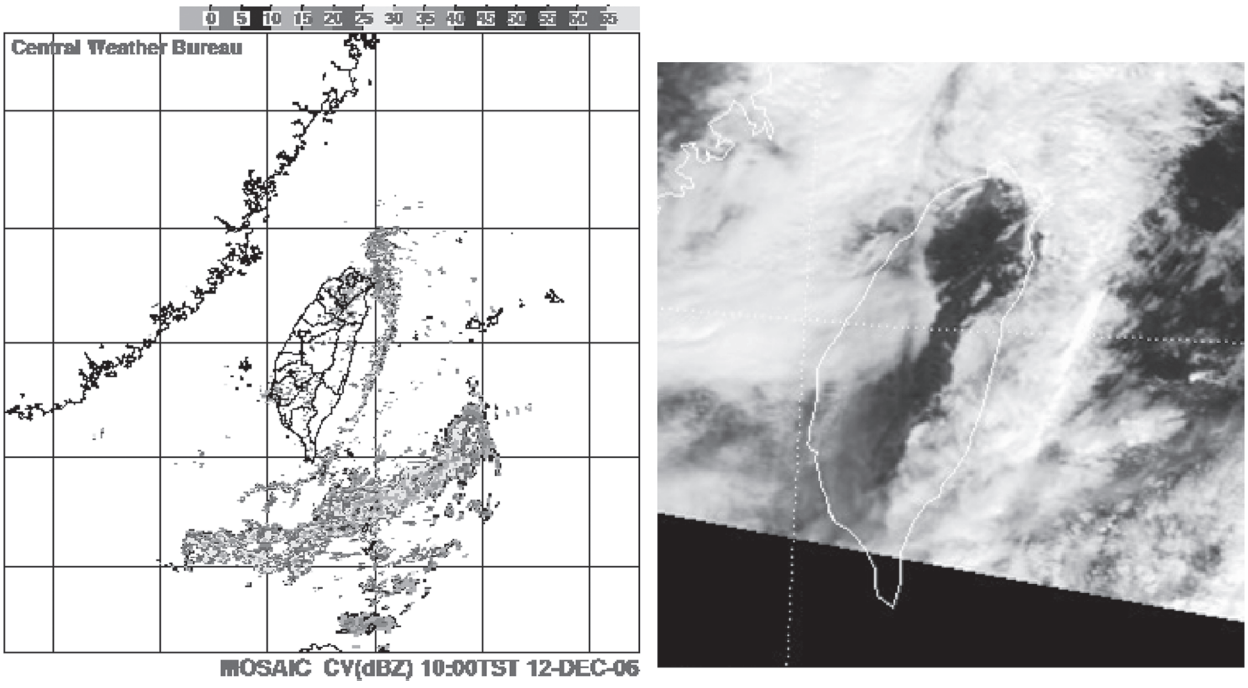

FIG. 8. (left) Weather radar image acquired at 0200 UTC 12 Dec 2006. (right) MODIS (*Terra*) image acquired at 0215 UTC 12 Dec 2006.

the weather radar image depicted in Fig. 7, which shows a broad band of heavy rain in the central and northern sections off the east coast of Taiwan and only a thin rainband consisting of several small rain cells in the southern section. When zooming in the ASAR image in the area southeast of Taiwan (not shown here) one can see radar signatures of several very small rain cells aligned parallel to the frontal line, but slightly offset from the frontal line toward the coast. They show up on the SAR image as small bright spots suggesting that the radar signatures are caused by scattering at raindrops in the atmosphere and not by scattering at the sea surface, where the rain drops impinging onto the sea surface change the small-scale sea surface roughness. The quasi-simultaneously acquired weather radar image shows small rain cells almost at the same locations, thus confirms our interpretation of the white spots being radar signatures of rain cells.

The plot depicted in Fig. 11 shows the simulated wind velocity (vectors) and wind speed (shading) calculated for the lowest level at 1400 UTC 11 December 2006. When comparing the measured sea surface wind speed in the coastal band off the southeast coast (Fig. 5, right panel) and the simulated one (Fig. 11), one notes a large difference. One could suspect that this difference is due to the fact that the algorithm by which the near-surface wind field is retrieved from the SAR image uses a wrong wind direction, which is not measured, but taken from the NCEP reanalysis data. NCEP has a coarse spatial resolution (0.5° longitude and latitude) and a coarse temporal resolution (3 h). If in reality the wind had blown in a more coast-parallel direction, then the retrieved wind speed would have come out to be slightly higher (1–2 m s^{-1}) because in this case the SAR antenna would have looked more in crosswind direction. But the difference is also likely because of deficiencies in the MM5 model to simulate the near-surface wind field at the south coast of Taiwan. Figure 11 also shows a large area of high wind speed to the south of the southern tip of Taiwan, which is in accordance with the wind field derived from the ASAR image (Fig. 5). This high wind speed zone could be a manifestation of a late development of a barrier jet, as the Coriolis acceleration takes some distance to speed up the airflow.

5. The 27 April 2007 event

a. Observations

Figure 12 (left panel) shows a section of a SAR image acquired by the ASAR onboard the *Envisat* satellite in the wide swath mode at 1355 UTC (2155 LST) on 27 April 2007 over the southern tip of Taiwan. The right panel shows the sea surface wind field derived from this ASAR image using the CMOD4 model and by taking the wind direction from the NCEP model. Visible on the wind field plot in the lower-right-hand section is the island of Lanyu as a dark patch, and in the upper-right-hand section (outside the area imaged by ASAR) is the

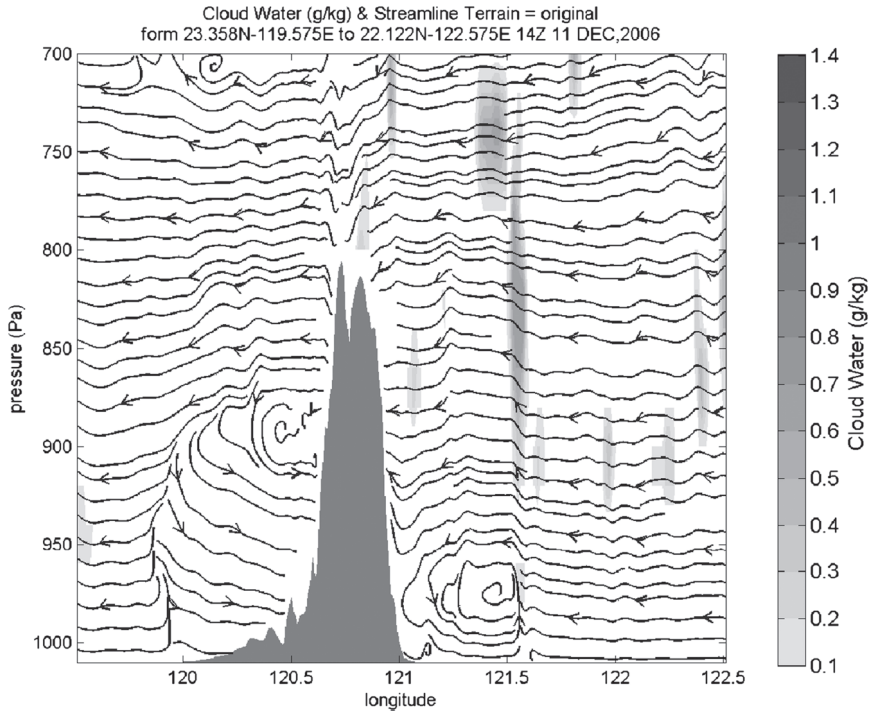

FIG. 9. Vertical cross section of the simulated streamlines and cloud water content (grayscale shading; g kg^{-1}) along a transect through southern Taiwan at 1400 UTC 11 Dec 2006.

island of Lutao as a smaller dark patch. The sea surface wind field derived from *QuikSCAT* data acquired at 0954 UTC 27 April 2007 (not reproduced here) shows east of the southern tip of Taiwan a synoptic-scale wind blowing with a speed between 5 and 8 m s^{-1} from a northeasterly direction. However, we infer from the direction of the wind shadow behind the island of Lanyu and from the direction of the gap winds on the western side of southern Taiwan visible on the ASAR image that the near-surface wind was blowing from a more easterly direction against the mountain range of southern Taiwan.

As on the ASAR image depicted in Fig. 5, the most noticeable feature is the dark area, about 20 km wide, stretching along the southeastern coast of Taiwan, indicating that the wind speed here was very low, about 3 m s^{-1}, which is much lower than the wind speed of the synoptic wind farther east (about 7 m s^{-1}). One could argue that here too the wind speed retrieved from the ASAR image is underestimated by the CMOD4 model because it uses an incorrect wind direction provided by the NCEP model. If we adhere to the barrier jet hypothesis and assume that in the dark area the wind was blowing parallel to the coast, then indeed the CMOD4 model would yield a slightly higher wind speed by about 1–2 m s^{-1}. But this small increase would not warrant associating this low wind speed area with a barrier jet.

A close inspection of the ASAR image in Fig. 12 reveals that small elliptical features are embedded in the frontal line, which suggests the presence a small rain cells. This interpretation is supported by the MODIS *Terra* image acquired at 0305 UTC 27 April 2007 (not reproduced here), which shows a narrow cloud band at the position of the frontal line. Also the weather radar image acquired at 0200 UTC on this day (not reproduced here) shows small rain cells in this area. Furthermore, the wind pattern visible on the ASAR image on the western side of southern Taiwan reveals that the wind at higher levels was blowing from an easterly direction and that the airflow of this easterly synoptic-scale wind was capable of passing the lower sections of the mountain range (less than 800 m high) but not the higher sections (over 1000 m high).

The radio sounding data acquired at 1200 UTC 27 April 2007 at Taipei and Ishigakijima show that aloft (above 1000 m) a westerly to northwesterly wind was blowing. The water temperature was 27°C and the air temperature at Ishigakijima was 24.2°C and at Taipei 26.6°C. The 850-hPa weather map shows a westerly wind aloft crossing central Taiwan.

b. Simulations

The results of the simulations carried out with the MM5 model at 0200 UTC 27 April 2007 event are

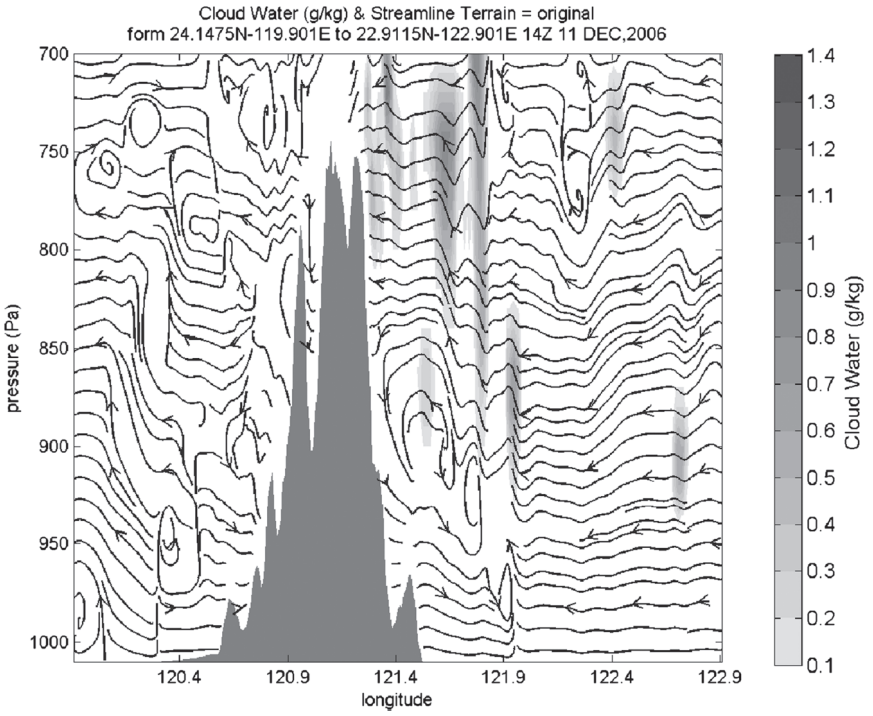

FIG. 10. Vertical cross section of the simulated streamlines and cloud water content (grayscale shading; g kg^{-1}) along a transect through central Taiwan at 1400 UTC 11 Dec 2006.

depicted in Figs. 13 and 14. Figure 13 shows the vertical cross section of the simulated streamlines and the cloud water content along a transect through central Taiwan. Here too a recirculation pattern is visible whose center is located at a very low level (250 m).

The simulated wind field calculated for the lowest level at 1400 UTC 27 April 2007 is depicted in Fig. 14. As with the simulated wind field for the previous event (Fig. 11) it shows at the southeast coast of Taiwan higher wind speeds than at the northeast coast, which would be indicative of a barrier jet. But this interpretation is in contradiction to the SAR image (Fig. 12) that shows a low wind speed band adjacent to the southeast coast of Taiwan.

6. The 30 September 2005 event

a. Observations

Figure 15 (left panel) shows an *Envisat* ASAR wide swath image acquired at 0148 UTC (0948 LST) on 30 September 2005 over Taiwan and the right panel a MODIS *Terra* cloud image acquired at 0255 UTC 30 September 2005. The area imaged by ASAR is 290 km by 330 km. It shows a convex frontal line that almost touches the northeast coast of Taiwan and that has at central Taiwan an offshore distance of 80 km. In the lower section of the ASAR image the island of Lutao is visible as a bright spot. The feature north of this island is very likely a sea surface signature of an oceanic vortex street generated by the interaction of the northward-flowing Kuroshio with this island. Figure 16 shows the sea surface wind field derived from *QuikSCAT* data, which were acquired at 2054 UTC 29 December 2005 (4 h and 54 min before the acquisition of the ASAR image). It shows that a northeasterly wind was blowing with a speed of about 8 m s^{-1} toward the east coast of Taiwan. In the central part of the east coast the wind component normal to the mountain range was about 4 m s^{-1}, while to the north and to the south the normal wind component was somewhat lower (to the south due to the change in wind direction and to the north due to the lower wind speed).

The radio sounding data acquired at 0000 UTC 30 September 2005 at Taipei show that at all levels the wind was always blowing from an easterly direction (no wind reversal aloft) and at Ishigakijima they show that at all levels the wind was blowing from a northeasterly direction. The water temperature was 29°C and the air temperature at Ishigakijima was 28.8°C and at Taipei 25.2°C. The 850-hPa weather map shows that aloft an easterly wind was blowing crossing central Taiwan.

b. Simulations

The results of the simulations carried out with the MM5 model at 0200 UTC 30 September 2005 event are

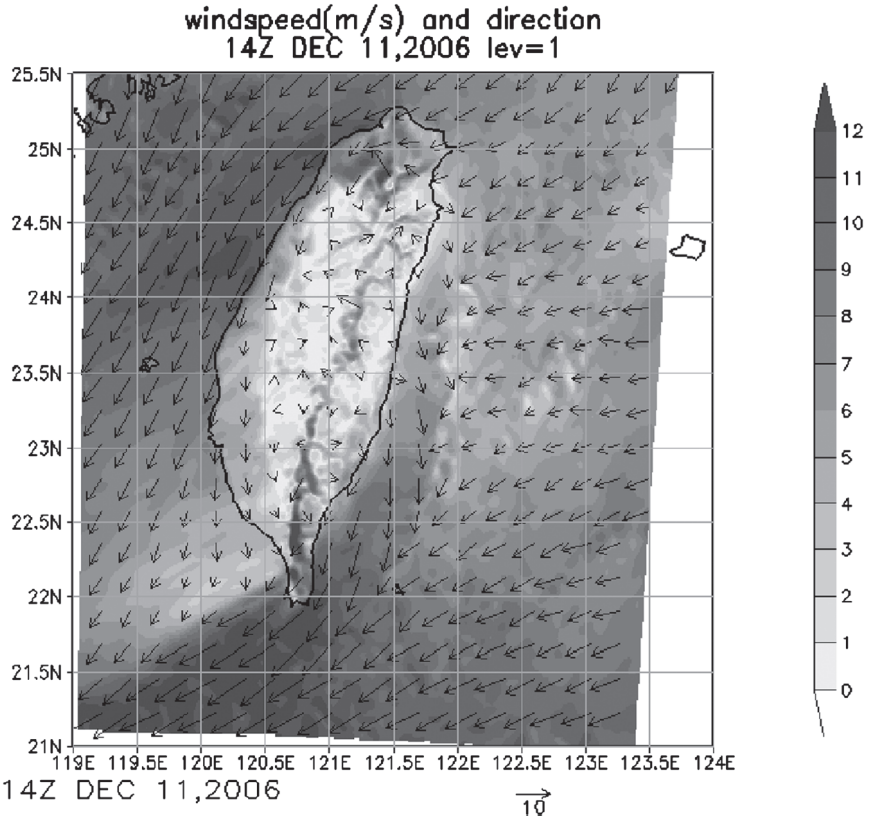

FIG. 11. Simulated wind velocity (vectors) and wind speed (grayscale shading; m s^{-1}) at the lowest level at 1400 UTC 11 Dec 2006.

depicted in Figs. 17–19. The plot depicted in Fig. 17 shows a vertical cross section of the simulated streamlines and of the cloud water content along a transect through northern Taiwan (same location as in Fig. 2). As in all previous plots of vertical profiles, also here a recirculation pattern is visible. The distance of the convergence line from the base of the mountain range is about 80 km, which agrees quite well with the distance retrieved from the ASAR image at this location.

The plot depicted in Fig. 18 shows the simulated wind velocity and wind speed calculated for the lowest level. It shows a northerly synoptic-scale wind blowing almost parallel to the coastline. No obvious convergence line off the east coast of Taiwan can be delineated on this plot. However, the wind field measured by *QuikSCAT* (Fig. 16) shows that everywhere along the east coast the wind had also a normal component to the mountain range. Thus the synoptic-scale wind must have interacted with the coastal mountain range leading to an offshore airflow. This interaction is strongest where the normal wind component is largest. This is confirmed by the MODIS cloud image depicted in Fig. 15 (right panel), which shows a convex cloud-free area adjacent the coast. Also the map of the integrated cloud water calculated from the MM5 model (Fig. 19) shows this convex pattern.

7. Discussion of the results

The numerical calculations carried out with the MM5 model for the four events discussed in the previous sections show that the frontal lines visible on the SAR images are generated by airflow blocking by the steep mountain range along the east coast of Taiwan. This has been one of the two hypothesis presented in the paper by Alpers et al. (2007) to explain the generation of frontal lines that are often visible on SAR images acquired over the east coast of Taiwan. A schematic plot illustrating the interaction of the reversed airflow with the onshore airflow of the synoptic-scale wind is depicted in Fig. 20 (applies for the case that aloft a westerly wind is blowing, as in the 18 January 1999 and 27 April 2007 events).

There is substantial observational evidence against the hypothesis that katabatic winds are responsible for the generation of the frontal lines visible on the SAR presented in sections 3–6 and in Alpers et al. (2007). The arguments against the katabatic wind hypothesis are as follows: 1) the persistence of cloud bands (18 January

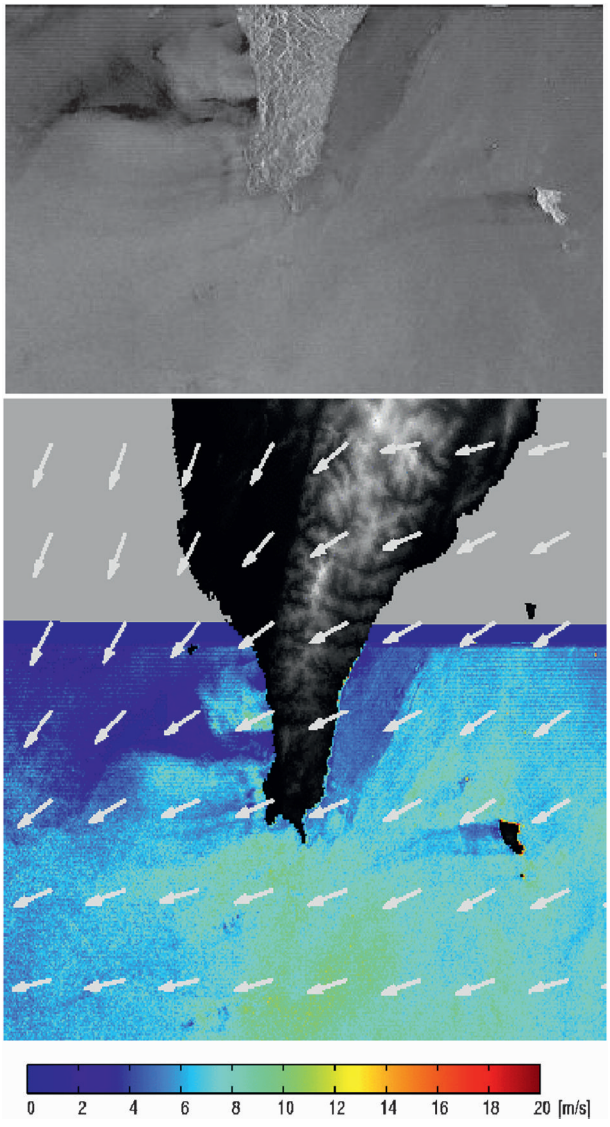

FIG. 12. (top) *Envisat* ASAR wide swath image acquired at 1355 UTC (2155 LST) 27 Apr 2007 over the southern tip of Taiwan. The imaged area is 150 km by 110 km. (bottom) Sea surface wind field derived from the ASAR image by using the CMOD4 wind scatterometer model and by taking the wind direction from the NCEP model. East of the southern tip of Taiwan, the island Lutao is visible.

1999 event) and rainbands (11 December 2006 event) over long time periods particularly at times when katabatic winds cannot be present; 2) the presence of clouds at the top of coastal mountain, which cannot be associated with the downslope katabatic winds; and 3) the large distance (up to 90 km) of the frontal lines from the base of the mountain range, the flow of cold air from the mountains of Taiwan associated with katabatic winds cannot reach such large distances. Furthermore, the airflow of katabatic winds is strongly affected by coastal topography leading to sea roughness patterns that have the form of tongues attached to the coastline. These ''wind tongues'' are generated by airflow funneled through coastal valleys onto the sea (see, e.g., Alpers et al. 1998). Typical offshore distances of katabatic winds at the east coast of Taiwan are 5–20 km. An example of an ASAR image showing this phenomenon will be given in the next section. In a detailed examination on the model results, we cannot find any evidence of strong nocturnal surface cooling over the terrain or subsequent emergence of katabatic wind of corresponding scales. Therefore, we discard the hypothesis that the katabatic wind is the main cause for the generation of the atmospheric frontal lines (Yu and Jou 2005). However, we cannot rule out the possibility that in some cases katabatic winds have a secondary or modulating effect on their generation and time evolution.

So, recirculation of blocked airflow by mountains is our favored mechanism. Such a mechanism has been investigated previously by Smolarkiewicz et al. (1988), Rasmussen et al. (1989), and Rasmussen and Smolarkiewicz (1993) to explain the generation of cloud bands that are often observed off the Hawaiian Island. However, contrary to the Hawaiian Island situation, in Taiwan the airflow is blocked by a medium–long but steep mountain range stretching over a length of approximately 350 km and having an average terrain height of 2500 m and a maximum height of 3952 m. The distance from the base to the peak of the Central Mountain Range of Taiwan is generally less than 50 km. Pierrehumbert and Wyman (1985) gave a comprehensive discussion on the effect of mountain blocking on upstream flow. They pointed out that the controlling factors of upstream deceleration of airflow are the Rossby number (Ro) and the Froude number (Fr). In the nonrotating limit, mountain blocking would cause a deceleration of the low-level onshore flow, which extends progressively farther upstream as time passes; but in the rotating case, the deceleration would attain a maximum extent on the order of the Rossby radius of deformation. Furthermore, in the nonrotating limit, Fr is the sole determining parameter, and the low-level onshore flow would decelerate to rest when $\mathrm{Fr} > 0.67$. Note that conventionally the Froude number is defined as

$$\mathrm{Fr} \equiv \frac{U}{h_m N}, \tag{1}$$

where U is the speed of the onshore flow, h_m is the mountain height, and N is the Brunt–Väisälä frequency, but in Pierrehumbert and Wyman (1985) it is defined inversely as $\mathrm{Fr} \equiv h_m N/U$.

In the following we try to understand whether the phenomenon observed in this study fits the upstream

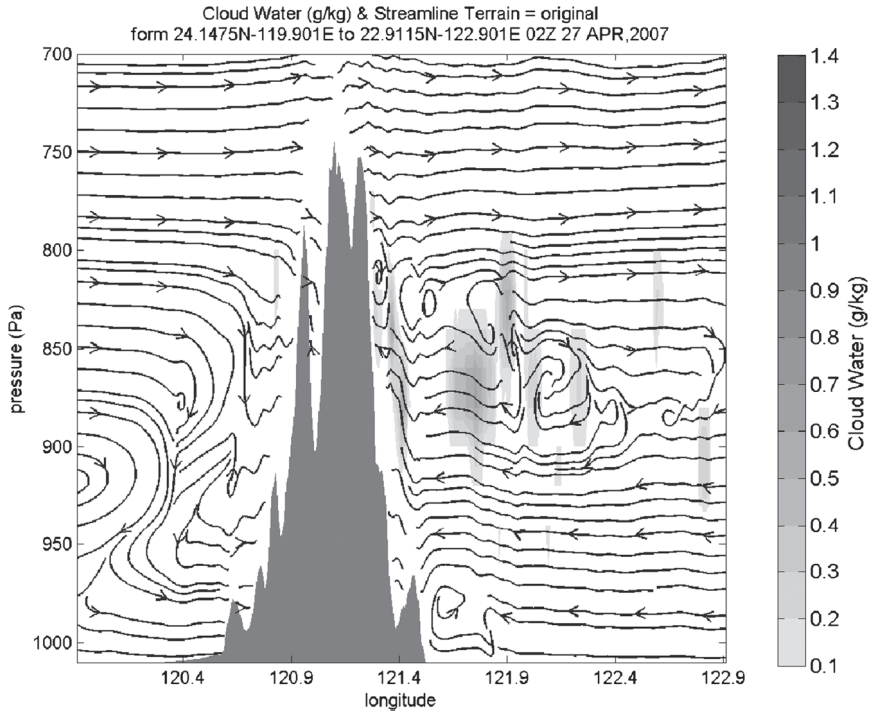

FIG. 13. Vertical cross section of the simulated streamlines and cloud water content (grayscale shading; g kg^{-1}) along a transect through central Taiwan at 0200 UTC 27 Apr 2007.

effect of mountain blocking described by Pierrehumbert and Wyman (1985), and whether the point of stagnation (the zero wind speed point) they mentioned demarcates the convergence line where the recirculation flow meets the onshore flow as we discussed. For the four cases presented above, Fr remains fairly constant at 0.4 ± 0.03 according to the sounding data at Hualien, or 0.4 ± 0.05 according to the NCEP reanalysis data at about 200 km off the east coast (representing the uninfluenced onshore flow). Obviously, such Froude numbers are below the criterion ($Fr > 0.67$) of stagnant flow for the nonrotating situation. In fact, for the spatial scale discussed here the Coriolis force should be effective. As the pressure builds up at the low level due to mountain blocking, a pressure gradient wind is established, directing outward to the ocean. But because of the Coriolis force the outward airflow will veer to the right (south in our case) and eventually form a semigeostrophic wind blowing parallel to the mountain range, as can be seen in Figs. 3, 11, and 14. The upstream extent of this deflected wind flow should exhibit the characteristics of the Rossby radius of deformation, which is defined as

$$L_R \equiv \frac{NH}{f}, \tag{2}$$

where f is the Coriolis parameter (around 6×10^{-5} s^{-1} for the latitude of Taiwan), and H is generally defined as the height of the flow. Note that if the thickness of the onshore flow is much higher than the mountain, it is unlikely that the upper part of the flow can also be blocked. Thus, in the following calculation we limit the value of H to be less than h_m.

For the 1999, 2005, and 2006 cases (discussed in sections 3, 6, and 4, respectively), we obtained L_R to be about ~370–380 km. Yet, the offshore distance of the actual convergence line ranges from 40 to 80 km only. For the 2007 case, L_R reduces to 200 km, but this is still much larger than the actual offshore distance of 20 km at the southern section of Taiwan. Note that, besides the main Central Mountain Range, there is also a smaller mountain range along the midsection of east coast, with a peak height of just over 1 km and average height of over 500 m (see the topography in Figs. 2, 10, and 15). If we assume this coastal mountain range produces a first line of blocking, then L_R would reduce to about 100 km. But this value is still too large to explain the observation. Note that such a recalculation was not performed for the 2007 case as the coastal mountain range vanishes at the southern section shown in Fig. 12. The concept of Rossby radius of deformation is conventionally regarded as a two-dimensional problem, and applies to mountains of very long dimension. We suspect the relatively short extent of the Central Mountain Range of Taiwan would allow the onshore airflow to splits and go

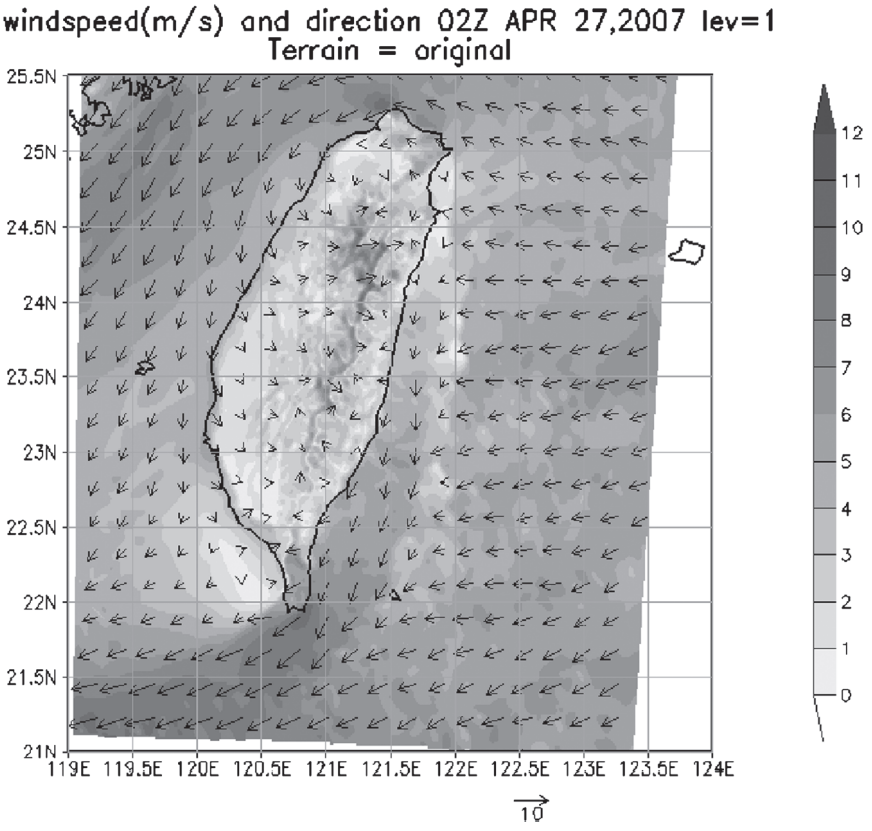

FIG. 14. Simulated wind velocity (vectors) and wind speed (grayscale shading; m s^{-1}) at the lowest level at 1400 UTC 11 Dec 2006.

around the island, thus ease up the blocking effect and shorten the distance of the stagnation point. Such three-dimensional flow patterns are indeed seen in the model simulations. It is interesting to note that L_R in Eq. (2) depends on the flow depth (or the mountain height if the airflow is thicker). For the 2007 case, the onshore synoptic flow is rather shallow (only up to the 900-hPa level), and indeed the offshore distance of the stagnation point is much shorter for this event.

We further analyze the blocking mechanism with the MM5 model by artificially lowering the mountain height as shown in Fig. 21. For the 1999 case, as the mountain height is halved, the recirculation roll not only reduces in size but also retreats toward the mountain base by about half the distance. The degree of this position shift seems to be consistent with Eq. (2). The recirculation roll continues to shrink and even becomes indiscernible when the mountain is lowered to one-quarter of the original heights under the current model resolution. The situation for the 2005 and 2006 cases is similar, which will not be repeated here. However, in the 2007 case (bottom panels of Fig. 21) the offshore distance of the convergence line does not change significantly when the mountain heights are halved. A possible explanation is that the depth of the onshore airflow is quite shallow in this particular event, reaching only about the 900-hPa level or halfway up the mountain. In such a situation the parameter H in Eq. (2) is the airflow depth, which remains constant. Note that the cloud band associated with the recirculation flow dissipated in the ½ height simulations and disappeared all together in those with ¼ mountain heights, indicating that the cloud band and the atmospheric front are indeed a consequence of mountain blocking.

According to Eq. (2), L_R should be independent of the wind speed, yet the offshore distance of the stagnation point does seem to vary from case to case or vary with the location, even though their values of L_R are very similar. For example, the frontal line often exhibits a convex shape (most clearly seen in Fig. 15), with an offshore distance that is the farthest in the central section of Taiwan and decreases to the north and to the south. It is reasonable to relate this phenomenon again with the three-dimensional structure of airflow around the mountain range because the relaxation of pressure gradient buildup should be more significant toward the ends of the mountain range. Such a change

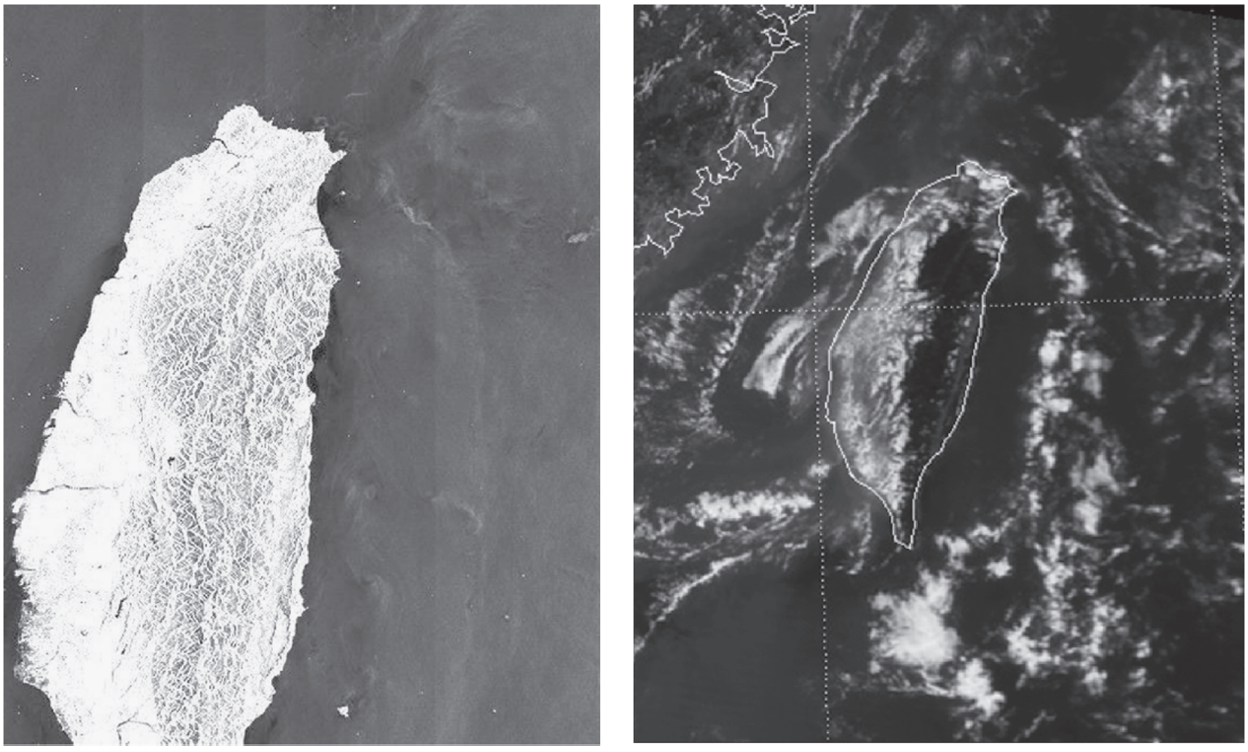

FIG. 15. (left) *Envisat* ASAR wide swath image acquired at 0148 UTC (0948 LST) 30 Sep 2005 over Taiwan. The central lower section of the image is the island of Lutao. The imaged area is 290 km × 330 km. (right) MODIS (*Terra*) cloud image acquired at 0255 UTC 30 Sep 2005.

of frontal-line distance is also generally consistent with the change of synoptic wind speed (more specifically, the component perpendicular to the mountain range) for the cases studied here.

Given enough time or distance, the acceleration by Coriolis force may generate high winds blowing into a southward direction parallel to the mountain range, which would be termed barrier jet (Parish 1982; Doyle 1997). Barrier jets have been observed previously in various mountainous environments, including the Sierra Nevada (Parish 1982), the Appalachians (Bell and Bosart 1988), Vancouver Island and the Olympic Mountains (Overland and Bond 1995), the west coast of the United States (Bond et al. 1996), the west coast of Taiwan (Li and Chen 1998), the southwest coast of Alaska (Overland and Bond 1993; Monaldo and Beal 2005; Loescher et al. 2006; Colle et al. 2006; Winstead et al. 2006), and along the California coast (Burk and Thompson 1996). A study of the climatology of barrier jets along the Alaskan coast carried out by Loescher et al. (2006) using Radarsat SAR images has shown that not only ''classical barrier jets'' are encountered in this region, but also ''hybrid barrier jets,'' ''shock barrier jets,'' and ''variable barrier jets.'' The coast-parallel roughness patterns visible on the SAR images presented in this paper and in Alpers et al. (2007) show some similarities with the wind pattern associated with variable barrier jets discussed by Loescher et al. (2006), but they still exhibit significant differences. On all of our SAR images we have not observed any distinct linear features near the coastline pointing into coast-parallel directions, which would be indicative for strong, barrier jet–type alongshore winds. On the contrary, the ASAR images of 18 January 1999 and 11 December 2006 (and several more SAR images presented in Alpers et al. 2007) rather show linear features directed away from the coastline, which is indicative of offshore winds. Furthermore, the darkish bands adjacent to the coastline visible on the SAR images of the 27 April 2007 and the 11 December 2006 events must be areas of low wind speed where the near sea surface wind must have a component directed away from the coastline (blowing in an easterly direction). This result seems not in accordance with barrier jet theory. As stated before, on all SAR images showing frontal lines off the east coast of Taiwan, we have found no evidence of strong winds blowing parallel to the coastline, which would be indicative for the presence of barrier jets.

Note that the simulated wind field of the 11 December 2001 event (Fig. 11) shows strong winds of more than

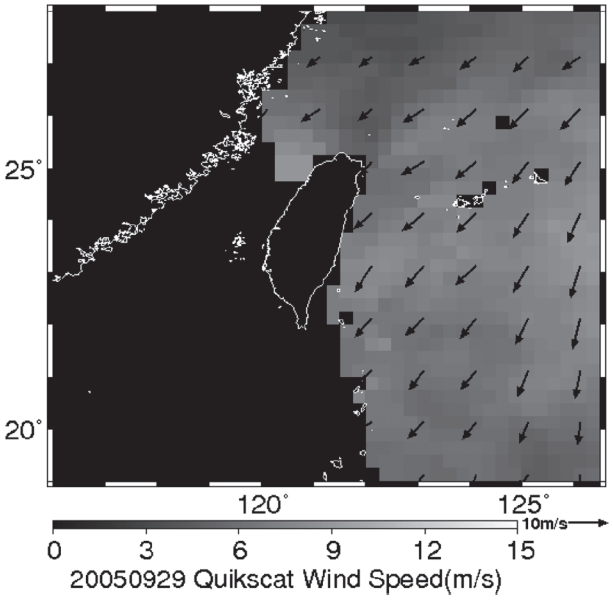

FIG. 16. Sea surface wind field derived from *QuikSCAT* data acquired at 2054 UTC 29 Sep 2005.

10 m s^{-1} at the very southeastern coast of Taiwan, while the ASAR image (Fig. 5) does not show this. The ASAR image shows a strong wind zone only at the very southern end of the island, which might indicate that in the model simulation the barrier jet develops somewhat too early. Often the coastal bands look darker (have lower NRCS values) than the synoptic-scale wind areas farther east indicating lower near-surface wind speed. Furthermore, the roughness patterns are much more inhomogeneous in these bands indicating large variations in wind speed. We attribute these variations mainly to the interactions of the synoptic-scale wind with the variable topography of the coastal mountain range and with the warm waters of the Kuroshio Current. Thus, we conclude that the simulations carried with the MM5 model reproduces quite well the observed offshore positions of the frontal lines off the east coast of Taiwan, but the model does not reproduce well the low wind speed bands at the southern end of the east coast of Taiwan as observed in the SAR images of 11 December 2006 (Fig. 5) and 27 April 2007 (Fig. 12). Possible causes for the unsatisfactory performance in these details include poor initial condition, particularly over the ocean, and insufficient spatial resolution of the model. There are also errors associated with the retrieval of SAR winds but, as discussed before, this influence should be minor.

Since none of the SAR images presented in sections 3–6 showed high wind speed jets along the coast, we discard the hypothesis that the frontal lines are the

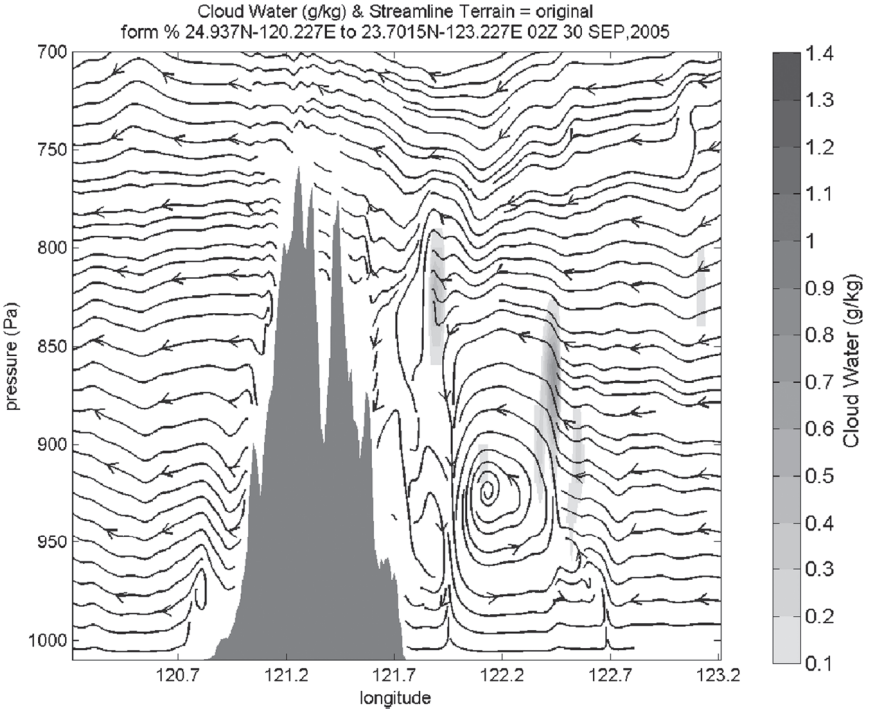

FIG. 17. Vertical cross section of the simulated streamlines and cloud water content (gray-scale shading; g kg^{-1}) along a transect through the northern section of Taiwan at 0200 UTC 30 Dec 2005.

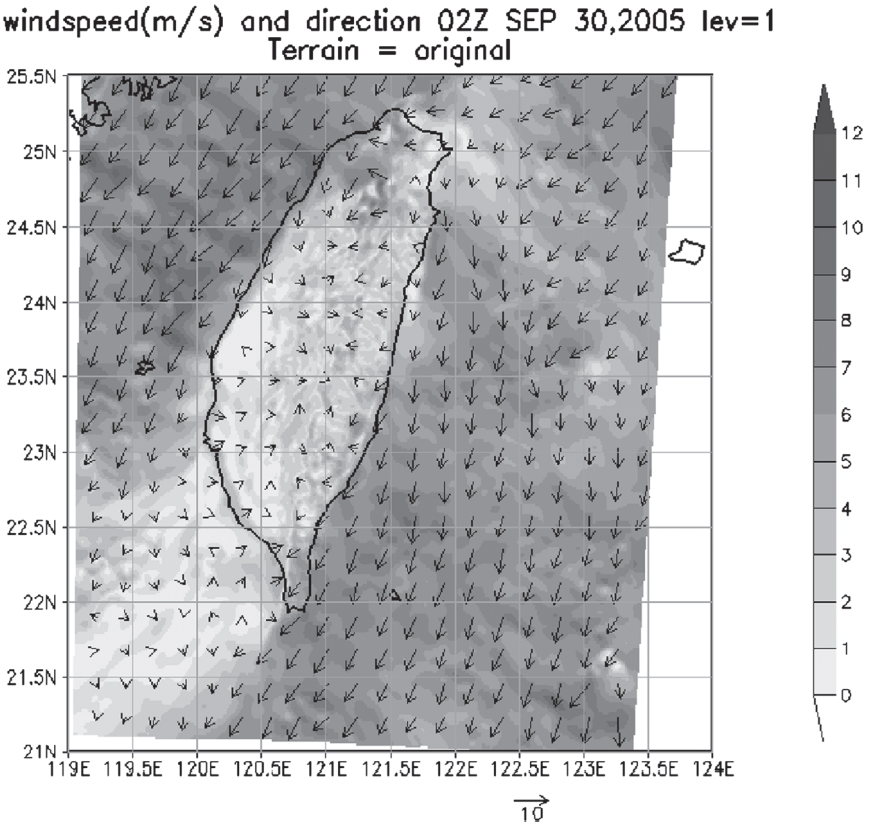

FIG. 18. Simulated wind velocity (vectors) and wind speed (grayscale shading; m s^{-1}) at the lowest at 0200 UTC 30 Sep 2005.

seaward boundaries of classical barrier jets. Such seaward boundaries should be quite broad, but they are observed to be quite sharp, which contradicts barrier jet theory. Unlike at the southwest coast of Alaska, the finite length of the barrier (the maintain range) has to be taken into account when modeling the interaction of the easterly airflow with the island of Taiwan. Thus, in our case, the theories used to describe the interaction of onshore flow with the island of Hawaii or with the mountain range of Alaska might not be applied. The interaction of easterly flow against the coastal mountain range of Taiwan, which has a quite variable topography, merits a separate theory.

8. An example of a katabatic wind front

As discussed in the previous section, it has sometimes been argued that frontal lines off the east coast of Taiwan could result from the collision of offshore airflow associated with land–sea breeze with onshore airflow associated with synoptic-scale easterly winds. Indeed, Yu and Jou (2005) have presented convincing evidence using Doppler radar and surface observations that this should be the case during their experiment carried out off the southeastern coast of Taiwan from 11 to 15 May 1998 during the mei-yu season. They observed that the frontal lines generally occurred 10–30 km offshore and exhibited a marked diurnal variation that was closely related to the coastal offshore flow developing at night. Such frontal lines are sometimes also observed on *ERS1/2* SAR and *Envisat* ASAR images when the meteorological conditions are favorable for the development of strong katabatic winds. Katabatic winds are encountered only late in the evening, at night, and early in the morning, and only when radiation weather prevails (i.e., when the sky is cloud free or almost cloud free such that radiation cooling can take place over the mountains; Alpers et al. 1998). To show that frontal lines caused by katabatic winds are quite different from those caused by recirculation of airflow discussed in sections 3–6, we present here for illustrative purposes one example. In Fig. 22, a SAR image is depicted which was acquired by *Envisat* ASAR in the Alternating Polarization (AP) mode late in the evening (at 2148 LST) on 10 May 2007. It shows the typical wind tongues adjacent to coastal valleys, which reach out onto the sea by 10–15 km. Thus,

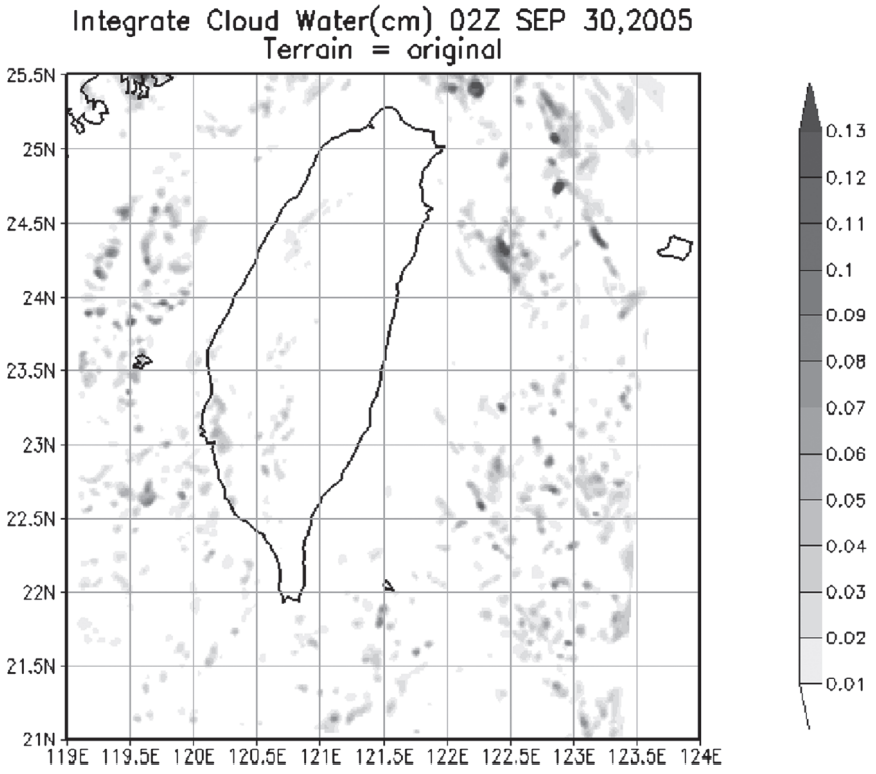

FIG. 19. Map of the simulated integrated cloud water content (cm) at 0200 UTC 30 Sep 2005.

the frontal line separating the katabatic wind field from the synoptic-scale wind field has an offshore distance which is much smaller than the offshore distances of frontal lines caused by recirculated airflow as discussed in the previous sections. At the time of ASAR data were taken, an easterly synoptic-scale wind of about 4 m s^{-1} was blowing against the mountain range of Taiwan. Furthermore, the MODIS *Terra* image (not reproduced here) taken during daytime (at 1035 LST on 10 May) shows cloud-free skies, which implies the absence of low-level convective clouds as required for the development of katabatic winds. Thus, we conclude from this example that the frontal lines discussed in sections 3–6 are not caused by katabatic winds. The main reason is that their offshore distances are too large to be caused by katabatic winds. In addition, in the case of katabatic

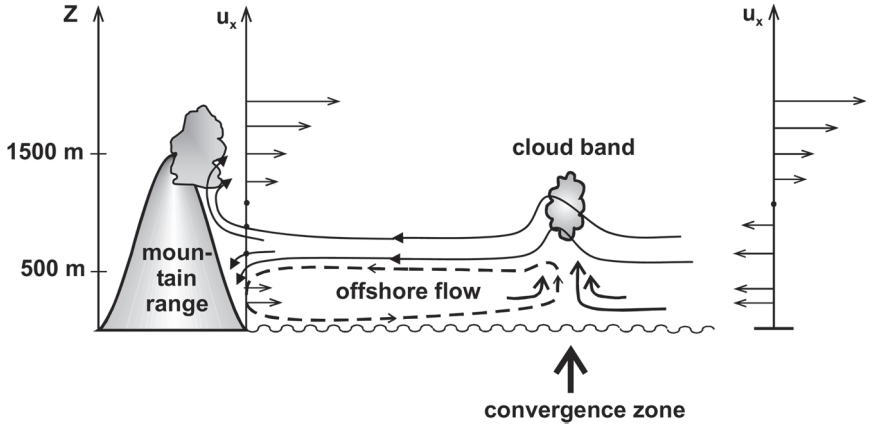

FIG. 20. Schematic plot of the airflow showing recirculation of air causing the formation of the coast-parallel atmospheric frontal line. The two vertical lines with the horizontal arrows attached denote the offshore components of the wind vector at the shoreline and east of the convergence line.

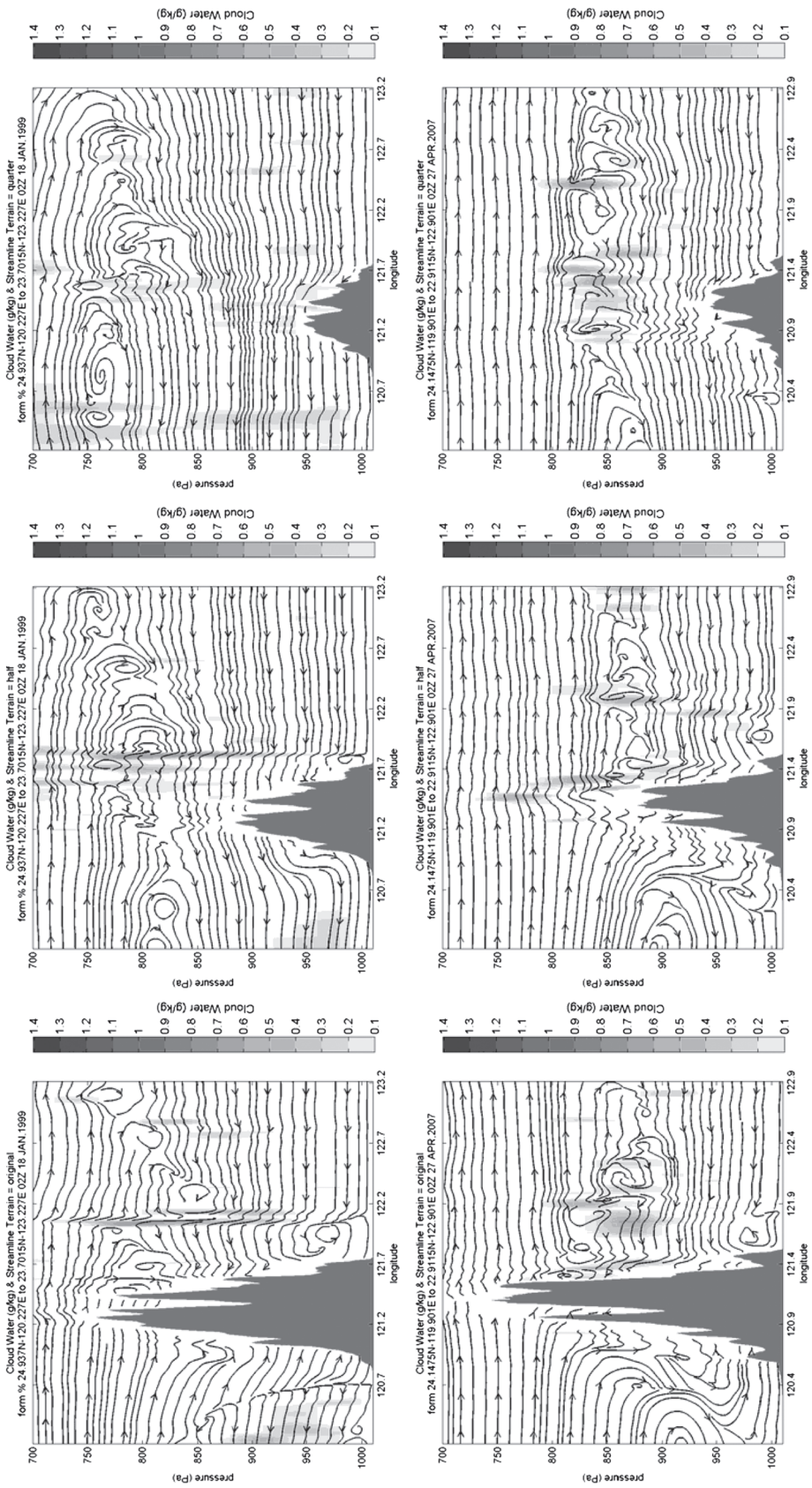

FIG. 21. Effect of mountain height on the recirculation pattern. (from left to right) Simulations using the original, one-half and one-quarter mountain heights. (top) The 18 Jan 1999 case [(left) as in Fig. 2], and (bottom) the 27 Apr 2007 case [(left) as in Fig. 13].

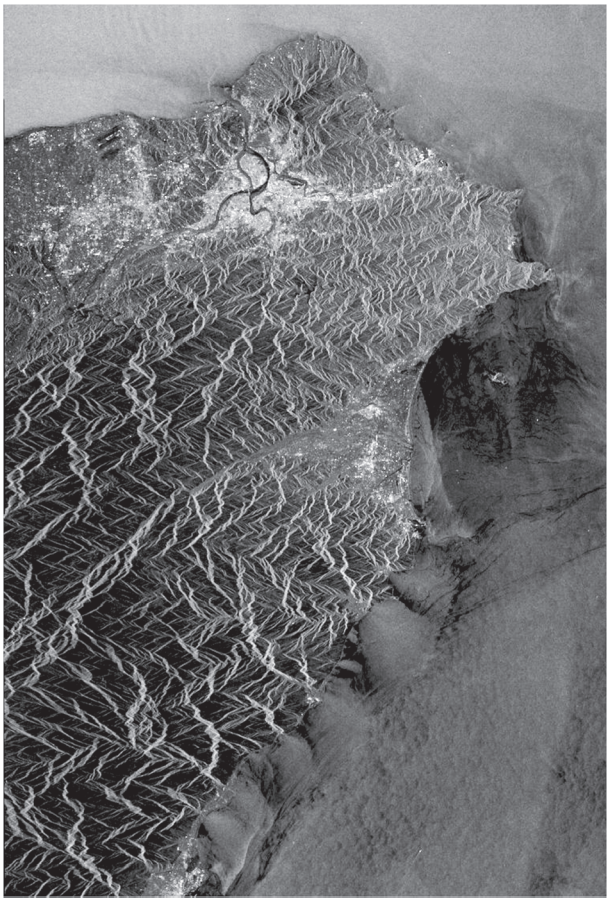

FIG. 22. *Envisat* ASAR AP image acquired at 1348 UTC (2148 LST) 10 May 2007 over the northeast coast of Taiwan. The imaged area is 100 km × 150 km. Sea surface signatures of katabatic winds attached to the coast are visible. The bright area in the upper section of the image is Taipei.

winds, where cold air flows downhill, no clouds should develop over the maintain range.

9. Conclusions and summary

Simulations carried out with the mesoscale atmospheric model MM5 show that the frontal lines often visible on SAR images acquired over the east coast of Taiwan are associated with a quasi-stationary low-level convergence zone generated by the interaction of two opposing airflows. Airflow of an easterly synoptic-scale wind blowing against the steep coastal mountain range of Taiwan interacts with the airflow reflected by the mountain range. The physical mechanism causing the generation of the frontal lines is similar to the one responsible for the formation of cloud bands off the Island of Hawaii as described by Smolarkiewicz et al. (1988).

In general, the MM5 model reproduces quite well the position of the frontal lines visible on the SAR images, the positions of the cloud bands visible on the optical images, and the location of the rainbands visible on weather radar images. However, the simulated horizontal wind field maps sometimes do not agree with SAR observations. In particular, the simulations often show strong barrier-parallel winds at the southeast coast of Taiwan. However, the SAR images that we have analyzed do not show these strong coast-parallel winds, which are typical for barrier jets. On the contrary, on two SAR images we have observed low wind speed bands adjacent to the coastline where the wind speed is by a factor of two lower than the wind speed in the area where the onshore synoptic-scale wind is blowing. The SAR images show further that the frontal (convergence) zones separating the two wind regimes are quite sharp, which is also not in agreement with classical barrier jet theory. Therefore, we conclude that the frontal lines that are often visible on synthetic aperture radar images acquired over the east coast of Taiwan cannot be associated with barrier jets. Furthermore, mainly because of their large offshore distance, they also cannot be associated with katabatic wind fronts. They are caused by recirculation of blocked airflow of an easterly synoptic-scale wind by the coastal mountain range.

Acknowledgments. We thank ESA for providing the *ERS-2* SAR image and the *Envisat* ASAR images free of charge within the frameworks of the ESA *Envisat* AO Project 418. Furthermore, we thank Knut-Frode Dagestad of the Nansen Environmental and Remote Sensing Center at Bergen, Norway, for providing the wind fields retrieved from the *Envisat* ASAR images. This research was supported by the research Grants NSC 95-2611-M-002-024-MY3, NSC 96-2475-M-002-009, NSC 96-2752-M-002-013-PAE, NSC 97-2111-M-002-014-MY3, NSC 97-2111-M-002-002, and NSC 97-2752-M-002-012.

REFERENCES

Alpers, W., and Ch. Melsheimer, 2005: Rainfall. *Synthetic Aperture Radar Marine User's Manual,* C. R. Jackson and J. R. Apel, Eds., NOAA/NESDIS, 355–371.

——, U. Pahl, and G. Gross, 1998: Katabatic wind fields in coastal areas studied by ERS-1 synthetic aperture radar imagery and numerical modeling. *J. Geophys. Res.,* **103,** 7875–7886.

——, J.-P. Chen, I.-I. Lin, and C.-C. Lien, 2007: Atmospheric fronts along the east coast of Taiwan studied by ERS synthetic aperture radar images. *J. Atmos. Sci.,* **64,** 922–937.

——, A. Ivanov, and J. Horstmann, 2009: Observations of bora events over the Adriatic Sea and Black Sea by spaceborne synthetic aperture radar. *Mon. Wea. Rev.,* **137,** 1150–1161.

Atlas, D., 1994: Origin of storm footprints on the sea seen by synthetic aperture radar. *Science,* **266,** 1364–1366.

Bell, G. D., and F. F. Bosart, 1988: Appalachian cold-air damming. *Mon. Wea. Rev.,* **116,** 137–161.

Bond, N. A., C. F. Mass, and J. E. Overland, 1996: Coastally trapped wind reversals along the United States west coast during the warm season. Part I: Climatology and temporal evolution. *Mon. Wea. Rev.,* **124,** 430–445.

Burk, S. D., and W. T. Thompson, 1996: The summertime low-level jet and marine boundary layer structure along the California Coast. *Mon. Wea. Rev.,* **124,** 668–686.

Colle, B. A., K. A. Loescher, G. S. Young, and N. S. Winstead, 2006: Climatology of barrier jets along the Alaskan Coast. Part II: Large-scale and sounding composites. *Mon. Wea. Rev.,* **134,** 454–477.

Doyle, J. D., 1997: The influence of mesoscale orography on a coastal jet and rainband. *Mon. Wea. Rev.,* **125,** 1465–1488.

Horstmann, J., and W. Koch, 2005: Comparison of SAR wind field retrieval algorithms to a numerical model utilizing ENVISAT ASAR data. *IEEE J. Oceanic Eng.,* **30** (3), 508–515, doi:10.1109/JOE.2005.857514.

Ivanov, A. Yu., W. Alpers, K. Ts. Litovchenko, M.-X. He, Q. Feng, M. Fang, and X.-H. Yan, 2004: Atmospheric front over the East China Sea studied by multi-sensor satellite and in-situ data. *J. Geophys. Res.,* **109,** C12001, doi:10.1029/2004JC002432.

Keller, W. C., V. Wismann, and W. Alpers, 1989: Tower-based measurements of the ocean C-band radar backscattering cross section. *J. Geophys. Res.,* **94,** 924–930.

Li, J., and Y. Chen, 1998: Barrier jets during TAMEX. *Mon. Wea. Rev.,* **126,** 959–971.

Loescher, K. A., G. S. Young, B. A. Colle, and N. S. Winstead, 2006: Climatology of barrier jets along the Alaskan coast. Part I: Spatial and temporal distributions. *Mon. Wea. Rev.,* **134,** 437–453.

Melsheimer, C., W. Alpers, and M. Gade, 2001: Simultaneous observations of rain cells over the ocean by the synthetic aperture radar aboard the ERS satellites and by surface-based weather radars. *J. Geophys. Res.,* **106,** 4665–4678.

Monaldo, F. M., and R. Beal, 2005: Wind speed and direction. *Synthetic Aperture Radar Marine User's Manual,* C. R. Jackson and J. R. Apel, Eds., NOAA/NESDIS, 305–320.

Overland, J. E., and N. A. Bond, 1993: The influence of coastal topography: The Yakutat storm. *Mon. Wea. Rev.,* **121,** 1388–1397.

——, and ——, 1995: Observations and scale analysis of coastal wind jets. *Mon. Wea. Rev.,* **123,** 2934–2941.

Parish, T. R., 1982: Barrier winds along the Sierra Nevada. *J. Appl. Meteor.,* **21,** 925–930.

Pierrehumbert, R. T., and B. Wyman, 1985: Upstream effects of mesoscale mountains. *J. Atmos. Sci.,* **42,** 977–1003.

Rasmussen, R. M., and P. K. Smolarkiewicz, 1993: On the dynamics of Hawaiian cloud bands. Part III: Local aspects. *J. Atmos. Sci.,* **50,** 1560–1572.

——, ——, and J. Warner, 1989: On the dynamics of Hawaiian cloud bands: Comparison of model results with observations and island climatology. *J. Atmos. Sci.,* **46,** 1589–1608.

Sikora, T. D., D. R. Thompson, G. S. Young, and N. S. Winstead, 1996: Evidence of a land breeze in an *ERS-1* SAR image of the New Jersey coastline. *Proc. Int. Geoscience and Remote Sensing Symp. 1996 (IGARSS'96),* Vol. 2, Lincoln, NE, IGARSS, 893–895.

Smolarkiewicz, P. K., R. M. Rasmussen, and T. L. Clark, 1988: On the dynamics of Hawaiian cloud bands: Island forcing. *J. Atmos. Sci.,* **45,** 1872–1905.

Stoffelen, A., and D. Anderson, 1997: Scatterometer data interpretation: Estimation and validation of the transfer function CMOD4. *J. Geophys. Res.,* **102,** 5767–5780.

van Vledder, G., and L. Holthuijsen, 1993: The directional response of ocean waves to turning winds. *J. Phys. Oceanogr.,* **23,** 177–192.

Winstead, N. S., B. Colle, and N. Bond, 2004: Synthetic Aperture Radar and high-resolution MM5 simulations of barrier jets in coastal Alaska. *Proc. Int. Geoscience and Remote Sensing Symp. 2004 (IGARSS'04),* Vol. 1, Anchorage, AK, IGARSS, 140–143.

——, and Coauthors, 2006: Using SAR remote sensing, field observations and models to better understand coastal flows in the Gulf of Alaska. *Bull. Amer. Meteor. Soc.,* **87,** 787–800.

Yu, C.-K., and B. J.-D. Jou, 2005: Radar observations of the diurnally forced off-shore convective lines along the southeastern coast of Taiwan. *Mon. Wea. Rev.,* **133,** 1613–1636.